PCCP

ROYAL SOCIETY OF CHEMISTRY

PAPER

View Article Online
View Journal

Check for updates

Cite this: DOI: 10.1039/d0cp03234d

Anchoring of palladium nanoparticles on N-doped mesoporous carbon†

Lisa Warczinski, *[a] Bin Hu, [bc] Till Eckhard, [b] Baoxiang Peng, [bc] Martin Muhler [bc] and Christof Hättig [a]

Received 16th June 2020,
Accepted 19th August 2020

DOI: 10.1039/d0cp03234d

rsc.li/pccp

Pd nanoparticles deposited on nitrogen-doped mesoporous carbon are promising catalysts for highly selective and effective catalytic hydrogenation reactions. To design and utilize these novel catalysts, it is essential to understand the effect of N doping on the metal–support interactions. A combined experimental (X-ray photoelectron spectroscopy) and computational (density functional theory) approach is used to identify preferential adsorption sites and to give detailed explanations of the corresponding metal–support interactions. Pyridinic N atoms turned out to be the preferential adsorption sites for Pd nanoparticles on nitrogen-doped mesoporous carbon, interacting through their lone pairs (LPs) with the Pd atoms *via* N-LP – Pd d_σ and N-LP – Pd s and Pd d_π – π^* charge transfer, which leads to a change in the Pd oxidation state. Our results evidence the existence of bifunctional palladium nanoparticles containing Pd^0 and Pd^{2+} centers.

Published on 19 August 2020. Downloaded by Ruhr Universitat Bochum on 9/18/2020 10:13:42 AM.

Introduction

Carbon materials are among the most commonly used support materials for metal nanoparticle catalysts. They are highly resistant to both acidic and basic media and as a support material for metal nanoparticles (NPs) they also facilitate an easy recovery of the metal. Another advantage of carbon materials is that their surface properties can be fine-tuned with great precision.[1] For industrial heterogeneous catalysis two carbon support materials have attracted tremendous attention: carbon nanotubes and mesoporous carbon. Carbon nanotubes are among the most intensively studied materials in surface chemistry in recent years. Due to their unique crystalline structure, carbon nanotubes show high thermal stability.[2] Mesoporous carbon is a novel promising support material in heterogeneous catalysis. With its irregular porosity, mesoporous carbon is characterized by a very large surface area and can be easily synthesized at a low cost.[3]

One main focus of carbon research is the modification of carbon materials. The influence of surface defects, functional groups and heteroatoms on the structure and functionality of carbon materials, in the first place on carbon nanotubes, has been addressed in several studies. It has been shown that these surface defects, functional groups and heteroatoms also affect the interaction between a carbon surface and deposited metal nanoparticles. Nitrogen and oxygen on the surface of carbon support materials change the properties of the supported metal nanoparticles. As a consequence, nitrogen- and oxygen-containing functional groups can be used to tune the dispersion, morphology, crystal structure, electronic structure, mobility/stability and the catalytic performance of the supported nanoparticles.[4]

One of the most important industrial applications of metal nanoparticles on carbon support materials in heterogeneous catalysis is the hydrogenation of aromatic compounds. For instance, the catalytic hydrogenation of chloronitrobenzenes produces chloroanilines, which are precursors for many important organic materials. The major side reaction, which reduces the selectivity of these hydrogenation reactions towards chloroanilines, is the process of dechlorination.[5] To improve the selectivity, dehalogenation inhibitors like quinoline have to be added to the reaction system. We aim at designing novel catalyst support materials with moderate to strong surface basicity, which seems to be a promising alternative to adding basic molecules to the hydrogenation reaction. A key step for accomplishing this goal is to fully understand the fundamental processes occurring on the catalyst surface.

The purpose of this study is to shed light on the properties of Pd nanoparticles deposited on nitrogen-doped mesoporous carbon (Pd/NMC) compared to Pd on nitrogen-free mesoporous carbon (Pd/CMC). We aim to identify the preferential adsorption sites of Pd and to give an in-depth insight into the effect of nitrogen doping on the corresponding metal–support interactions.

[a] Chair of Theoretical Chemistry, Ruhr-University Bochum, 44780 Bochum, Germany. E-mail: lisa.warczinski@rub.de
[b] Laboratory of Industrial Chemistry, Ruhr-University Bochum, 44780 Bochum, Germany
[c] Max Planck Institute for Chemical Energy Conversion, 45470 Mülheim a.d. Ruhr, Germany

† Electronic supplementary information (ESI) available. See DOI: 10.1039/d0cp03234d

Published on 19 August 2020. Downloaded by Ruhr Universitat Bochum on 9/18/2020 10:13:42 AM.

For this purpose we combine experimental X-ray photoelectron spectroscopy (XPS) with a computational density functional theory (DFT) study. As theoretical model systems, we use a Pd_{21} cluster on a hydrogen terminated graphene layer, which has successfully been used as a model system for Pd/CMC in a previous study.[6]

Methodology

Synthesis of mesoporous carbon

Mesoporous carbon (CMC) was prepared from fructose (99% ADM) using $ZnCl_2$ as the template and catalyst.[7] N-Containing mesoporous carbon (NMC) was synthesized *via* carbonization of melamine (99%, Sigma-Aldrich) and formaldehyde (37 wt% in water, Sigma-Aldrich) using $CaCl_2$ (>95%, Fluka) as the template according to a previous report.[3] The as-prepared NMC and CMC were purified using a 1.5 M HNO_3 aqueous solution at room temperature for 72 h, followed by washing and filtration in deionized water several times until the pH of the filtrate became neutral. The purified NMC and CMC were dried at 80 °C overnight and ground for further use.

Catalyst preparation

Pd/NMC and Pd/CMC were prepared using a sol-immobilization method. Briefly, an aqueous solution of $PdCl_2$ (99%, Sigma-Aldrich) of the desired concentration was prepared. Subsequently, a polyvinyl alcohol (PVA) solution (1 wt%, M_W = 9000–10 000 g mol^{-1}) was added (PVA/Pd (wt/wt) = 1.2). Afterwards, a freshly prepared $NaBH_4$ aqueous solution (0.1 M, 10 times excess) was added, which immediately formed a dark-brown colloidal solution containing the Pd nanoparticles. As $NaBH_4$ is a very strong reducing agent, the complete reduction of the Pd^{2+} precursor to Pd^0 has been clearly demonstrated *via* UV-vis spectroscopy after the addition of $NaBH_4$ as reported in the literature.[8,9] After 30 min of sol generation, the powder support was added into the dark-brown colloidal solution at a proper pH under vigorous stirring. The required amount of the support was calculated to achieve a Pd loading of 1 wt%. After 2 h, the catalyst was obtained after filtration, washing with distilled water several times to remove boron and chloride, and drying at 80 °C overnight.

The supported catalysts and mesoporous supports were characterized *via* N_2 physisorption, XRD, and TEM and their properties have been reported in a previous study.[10] In brief, CMC and NMC exhibited comparable mesoporous structures, for example, similar average pore sizes of 5.0 and 4.9 nm, pore volumes of 1.2 and 0.7 cm^3 g^{-1}, and specific surface areas of 997 and 657 m^2 g^{-1}, respectively (Table S1, ESI†). After the deposition of Pd, the pore sizes, pore volumes, and BET surface areas of both catalysts were slightly decreased compared with those of the parent materials. The actual Pd loadings of the catalysts were found to be *ca.* 1.0 wt%. Compared with Pd/CMC, no significant Pd reflections were identified for Pd/NMC *via* XRD (Fig. S1, ESI†), suggesting higher Pd dispersion on NMC and the crucial role of N atoms as strong anchoring sites for Pd nanoparticles. The mean Pd particle sizes for Pd/NMC and Pd/CMC were rather similar amounting to 3.4 and 4.2 nm, respectively (Fig. S2, ESI†), allowing a direct comparison of metal–support interactions, excluding the effect of particle size.

X-ray photoelectron spectroscopy

X-ray photoelectron spectroscopy (XPS) measurements were performed in an ultrahigh vacuum setup equipped with a high-resolution Gammadata Scienta SES 2002 analyzer. A monochromatic Al Kα X-ray source (1486.6 eV, the anode operating at 14.5 kV and 30.5 mA) was used as the incident radiation source. The pressure inside the measuring chamber was kept in the range of 3.5 to 7 × 10^{-10} mbar during each measurement. The slit width of the analyzer was set at 0.3 mm and the pass energy was fixed at 200 eV for all measurements. The overall energy was better than 0.5 eV. Charging effects due to the insufficient conductivity of the carbon materials were mediated by using a flood gun (SPECS). All spectra were calibrated based on the C 1s binding energy of 284.5 eV. The CASA XPS program was used to analyze the XPS spectra, and a mixed Gaussian–Lorentzian function and Shirley background subtraction were applied in the fitting of the XPS data. The XPS survey spectra of the catalysts verified the presence of C, N, O, and Pd as well as the absence of B and Cl residues (Fig. S3, ESI†). Elemental analysis and XPS results demonstrated similar bulk and surface N abundances in NMC and Pd/NMC (Table S2, ESI†), indicating a homogenous distribution of N in NMC. Furthermore, CMC and Pd/CMC exhibit comparable but slightly higher surface oxygen contents compared to NMC and Pd/NMC (Table S2, ESI†).

Computational methods and model systems

The quantum chemical calculations were performed at the level of density functional theory (DFT) with the TPSS[11]/def2-SVP[12] functional and basis set and carried out using the TURBOMOLE[13] program package. For the palladium atoms Stuttgart–Cologne effective core potentials (def2-ecp)[14] were employed. All calculations include the multipole accelerated resolution of identity (MARI-J)[15] approximation with optimized auxiliary basis sets[16] and Grimme's D3[17] correction for London dispersion interactions.

To obtain an insight into the role of dispersion on the binding energies, single point energies were calculated with and without the D3 correction. Zero-point vibrational energy (ZPVE) corrections from the vibrational analysis were added to the energy differences.

To study the details of the electronic structure natural population analyses (NPAs)[18] were performed. As the π-system of the different support materials can be well described using Hückel theory, we also looked at Hückel-based population analyses. Furthermore, we calculated electron densities, generated electron density difference plots and visualized intrinsic bond orbitals (IBOs),[19] for which we used a 1s1p1d subset of the atomic orbitals in the cc-pVTZ-PP basis set for Pd.[20] To validate the experimental N 1s and Pd 3d XPS spectra, we calculated the density of states (DOS) based on a Mulliken

 This journal is © the Owner Societies 2020

Published on 19 August 2020. Downloaded by Ruhr Universitat Bochum on 9/18/2020 10:13:42 AM.

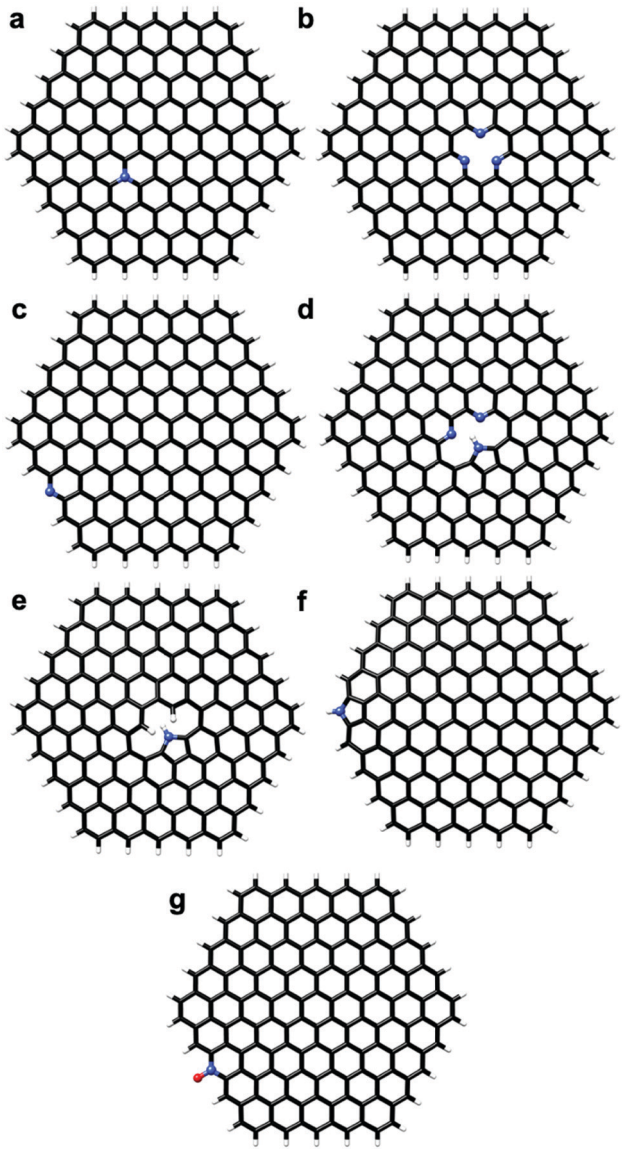


Fig. 1 Model systems for the NMC support material: (a) graphitic N; (b) pyridinic N b; (c) pyridinic N c; (d) pyrrolic N d; (e) pyrrolic N e; (f) pyrrolic N f; and (g) N–O-like N.

population analysis,[21] for Pd with a full electron ansatz (SVPall[22]). The absolute orbital energies are usually far away from experimental ionization energies. However, the Kohn–Sham eigenvalues provide a good estimate of the core level binding energy shifts.[23] Therefore, qualitative trends and energy differences for significantly different functional groups should be in good agreement with the experiment. Previously, it was shown that also the ΔSCF method can be used to accurately estimate N 1s core level binding energies.[24,25]

To model the Pd/CMC system we chose a Pd_{21} cluster on a hydrogen terminated graphene layer of 150 carbon atoms, which proved to be a reasonable choice in a previous study.[6] For the NMC systems we set up seven support material models for four different N atom types: graphitic N, pyridinic N, pyrrolic N and N–O like species (compare Fig. 1).

In the model for graphitic N, one C atom in the graphene layer was substituted by a N atom (compare Fig. 1a). For pyridinic N several different atomic arrangements would be possible. Based on a 2D TOF-SIMS study, which shows that pyridinic N atoms are usually distributed in domains,[26] we chose a support model system with a high density of pyridinic N, *i.e.* a model including a one C atom vacancy surrounded by three pyridinic N atoms (pyridinic b; compare Fig. 1b). As the three pyridinic nitrogen atoms show slightly different N 1s orbital energies, we set up a second support model for pyridinic N (one N atom replacing a C–H group at the edge of the graphene sheet; pyridinic c; compare Fig. 1c), which was used for calibrating the DOS calculations. Based on the results of a previous study, which show that the N 1s binding energies of pyridinic N atoms at different positions in the support material do not significantly differ from each other,[27] this should not introduce any significant uncertainty.

Furthermore it was shown that pyrrolic N atoms at different positions in the support material do show significantly different N 1s binding energies.[27] Accordingly, we set up three different support material models for pyrrolic N: (1) a one C atom vacancy surrounded by one pyrrolic N–H group and two pyridinic N atoms (pyrrolic d; compare Fig. 1d), (2) a one C atom vacancy surrounded by one pyrrolic N–H group and two C–H groups (pyrrolic e; compare Fig. 1e), and (3) a five-membered ring at the edge of the graphene sheet including a N–H group (pyrrolic f; compare Fig. 1f).

For the N–O-like species a model system of a N–O group replacing a C–H group at the edge of the graphene sheet was set up (compare Fig. 1g).

As the pyridine-like support model c, the pyrrole-like support models e and f and the model for the N–O-like nitrogen atom contain functional groups that are located on the edges of the support material, which would introduce undesired side effects in the geometry of the supported nanoparticles, these systems have only been considered for the DOS calculations and not as support materials for the Pd_{21} clusters.

The most stable structures of the support models as well as of Pd_{21} on the different support materials were determined *via* ground-state geometry optimizations. The model system for Pd/CMC is shown in Fig. 1. For Pd/NMC two different graphitic structures, two different pyridinic structures (both on the pyridinic support model b), and one pyrrolic structure (for the pyrrolic support model d) were investigated (compare Fig. 2–5).

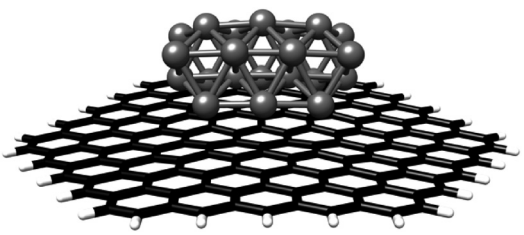


Fig. 2 Most stable structure of Pd_{21} on N-free carbon support (the model for Pd/CMC).

Published on 19 August 2020. Downloaded by Ruhr Universitat Bochum on 9/18/2020 10:13:42 AM.

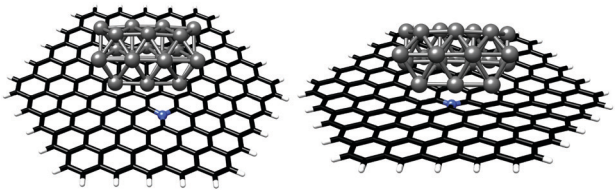


Fig. 3 Most stable structures of Pd_{21} on graphitic N carbon support: 1 (left; graphitic N on the side of Pd_{21}) and 2 (right; graphitic N below Pd_{21}) (models for Pd/NMC).

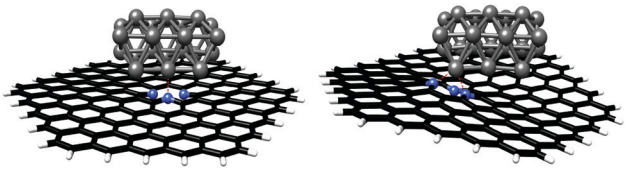


Fig. 4 Most stable structures of Pd_{21} on pyridinic N carbon support b: 1 (left; one pyridinic N connected to Pd_{21}) and 2 (right; two pyridinic N connected to Pd_{21}) (models for Pd/NMC).

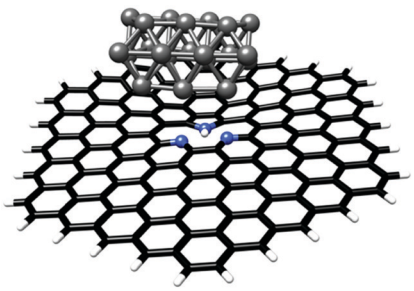


Fig. 5 Most stable structure of Pd_{21} on pyrrolic N carbon support d (model for Pd/NMC).

It has been well established by combined experimental and DFT studies that the oxygen functionalization of carbon nanotubes enhances the binding energy of Pd;[28–30] however, the interaction between Pd and surface oxygen is relatively weak.[28] Furthermore, considering the similar surface oxygen contents in Pd/CMC and Pd/NMC (Table S2, ESI†) and the same type of oxygen functional groups originated from the HNO_3 treatment, the influence of surface oxygen is neglected in the present study.

Results and discussion

Preferential adsorption sites

The N 1s core level XPS spectra of NMC and Pd/NMC are presented in Fig. 6. The deconvoluted N 1s spectrum of NMC reveals that nitrogen is embedded into the carbon structure in four different forms.[3,31] The first peak at 398.0 eV refers to the pyridine-like N atoms (N1). The second peak at 399.8 eV (N2) is tentatively assigned to N atoms in the pyrrole-like configuration, but considering previous studies[32] this may need to be further confirmed. The third peak at 401.0 eV (N3) can be assigned to quaternary-like N atoms, and the fourth peak at

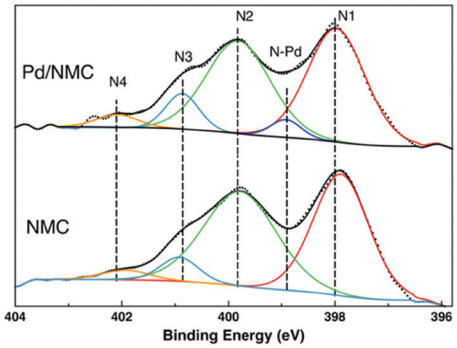


Fig. 6 N 1s regions of the deconvoluted XPS results for NMC and Pd/NMC.

Table 1 N 1s binding energies (eV) for the different N species

Model system	Calibrated DOS calculation	Experimental value
Pyridinic b	397.6–397.9	N1, 398.0
Pyridinic c	398.0	N1, 398.0
Pyrrolic d	399.0	N2, 399.8
Pyrrolic e	400.1	N2, 399.8
Pyrrolic f	400.1	N2, 399.8
Graphitic	401.5	N3, 401.0
N–O-like	402.0	N4, 402.0

402.0 eV (N4) to oxidized or NO-like N atoms.[33] This can further be validated by the N 1s binding energies obtained from our DOS calculations. The total DOS energies differ from the experimental results by an approximately constant shift of about 14 eV. Therefore, we used the pyridinic support model c to calibrate the calculations and shifted all the calculated binding energies by 14.3 eV (compare Table 1.). The energy trend and the energy differences between the different nitrogen species match very well. There are debates on whether pyrrolic and graphitic N can be distinguished in literature reports.[32] Because of the much better deconvoluted results as well as the better agreement of binding energies between the experimental and calculated values (Table 1), we decided to use 4 peaks for the N 1s XPS deconvolution in the present study.

The relative chemical abundance of each N functional group on the NMC surface was determined from the XPS data using tabulated theoretical photoelectron cross sections[34] and is summarized in Table 2. It shows that the embedded N is mainly in the state of pyridinic (N1, 45%) and pyrrolic (N2, 46.1%) groups, which are basic. The overall N abundance, especially the abundance of the N1 species, slightly decreases due to Pd loading, suggesting that pyridinic nitrogen species are probably the preferential anchoring sites for Pd NPs.

Table 2 Relative abundance (%) of the components in the N 1s spectra

Sample	Component/binding energy (eV)			
	N1	N2	N3	N4
	398.0	399.8	401.0	402.0
NMC	45.0	46.1	6.0	3.0
Pd/NMC	41.1	44.5	7.6	3.3

This journal is © the Owner Societies 2020

Published on 19 August 2020. Downloaded by Ruhr Universitat Bochum on 9/18/2020 10:13:42 AM.

Table 3 Calculated adsorption energies for the different Pd_{21} systems shown in Fig. 2–5

Model system	Adsorption energy with D3 (kJ mol^{-1})	Adsorption energy without D3 (kJ mol^{-1})	Dispersion energy (kJ mol^{-1})	Dispersion contribution (%)
Pd_{21}/carbon support	549.7	248.2	301.5	54.9
Pd_{21}/graphitic N support 1	574.3	278.1	296.2	51.6
Pd_{21}/graphitic N support 2	607.9	296.9	311.0	51.2
Pd_{21}/pyridinic N support 1	657.4	367.5	289.9	44.1
Pd_{21}/pyridinic N support 2	704.8	401.1	303.7	43.1
Pd_{21}/pyrrolic N support	579.1	272.2	306.9	53.0

To validate this experimental observation, we calculated the adsorption energies for the different Pd_{21} systems shown in Fig. 2–5. The results are listed in Table 3.

In general, N doping increases the adsorption energy of the Pd_{21} cluster on the carbon support material. This effect is, in the first place, of covalent character, as it was previously reported for the interaction of platinum nanoparticles with nitrogen-doped carbon support materials.[35] For the graphitic system, the configuration in which Pd_{21} is located directly over the N atom (graphitic N support 2, compare Fig. 3) is more stable than the configuration with the N atom on the side of the cluster (graphitic N support 1, compare Fig. 3). The pyrrolic N system (compare Fig. 5) behaves very similar to the graphitic N support 1 system.

The adsorption energies for the pyridinic systems are significantly higher. The highest adsorption energy can be observed for the configuration in which two pyridinic N atoms interact with one Pd atom (pyridinic N support 2, compare Fig. 4).

This confirms that pyridinic nitrogen species should be the preferential anchoring sites for Pd NPs on NMC, which is in agreement with previous reports suggesting that N-functionalized carbon materials can effectively anchor and stabilize the supported metal NPs.[36,37]

Details of the metal–support interactions

To understand the details of the previously described metal–support interactions, we calculated the electron densities for Pd_{21} on the graphitic N support 2, on the pyridinic N support 2 and on the pyrrolic N support. The corresponding electron density difference plots are shown in Fig. 8–10. For comparison, we reproduce the electron density difference plot for the N-free system from our previous study[6] (compare Fig. 7), showing that the electron density is shifted from the lower layer of the cluster to the Pd–C connecting lines. This indicates directed partially covalent metal–support interactions.

In the plot for the graphitic N support 2 shown in Fig. 8 no direct Pd–N bond can be observed. However, close to the graphitic N atom even more electron density is shifted to the Pd–C connecting lines compared to the N-free carbon support. This is in agreement with our result that the binding of Pd_{21} on N-doped support materials is more covalent. To explain this phenomenon, we performed a natural population analysis for the Pd_{21}/graphitic N support 2 model system as well as a Hückel-based population analysis for the support material. Based on these results, the stronger covalent Pd–C binding can be explained by two facts: (1) The graphitic N atom brings in an additional electron, which in the interacting system is (partially) located on the Pd_{21} cluster. The, in general, positive

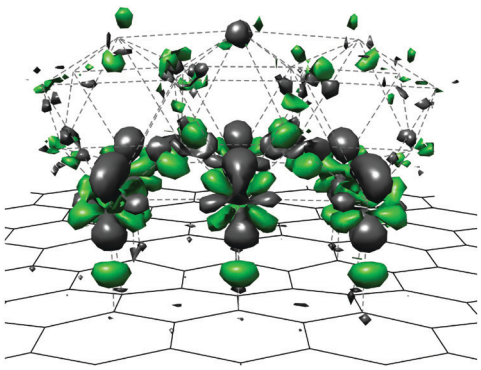


Fig. 7 Change in the electron density induced by the interaction between the Pd_{21} cluster and the N-free support material. Density gain is colored in green; density loss is in grey.

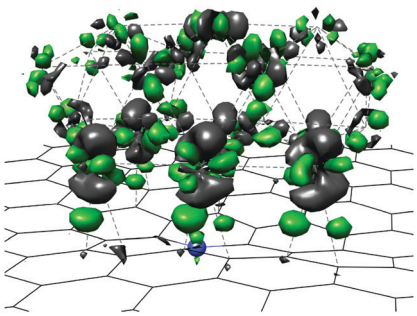


Fig. 8 Change in the electron density induced by the interaction between the Pd_{21} cluster and the graphitic N support material 2. Density gain is colored in green; density loss is in grey.

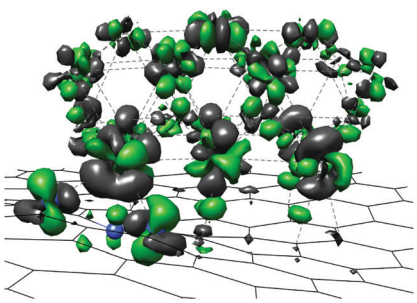


Fig. 9 Change in the electron density induced by the interaction between the Pd_{21} cluster and the pyridinic N support material 2. Density gain is colored in green; density loss is in grey.

Published on 19 August 2020. Downloaded by Ruhr Universitat Bochum on 9/18/2020 10:13:42 AM.

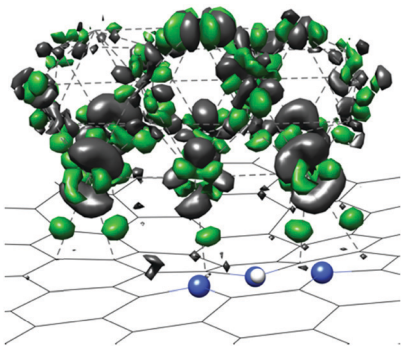


Fig. 10 Change in the electron density induced by the interaction between the Pd_{21} cluster and the pyrrolic N support material. Density gain is colored in green; density loss is in grey.

charge of the carbon supported Pd_{21} cluster is decreased. (2) The graphitic N atom and the neighboring C atoms are positively charged, which leads to an additional electrostatic contribution to the binding energy.

The plot for the pyrrolic N support system in Fig. 10 is very similar to that for graphitic N support 2. Also for this system no direct Pd–N bond and a stronger electron density shift to the Pd–C connecting lines compared to the N-free carbon support can be observed. However, this effect is slightly smaller compared to the effect of the graphitic N support 2 and can mainly be explained by the induced positive charge at the neighboring carbon atoms.

The plot for the pyridinic N support 2 (compare Fig. 9) shows a much more complicated electron density difference at the two pyridinic N atoms bound to the Pd_{21} cluster. This special structure can be explained with the help of an intrinsic bond orbital analysis. Each pyridinic N atom possesses a lone pair (LP), located in an sp^2-orbital lying in the support plane. For the two pyridinic N atoms directly bound to the Pd_{21} cluster this LP sp^2-orbital is tilted up by around 5° towards the cluster (compare Fig. 11), which is associated with an N-LP – Pd d_σ and an N-LP – Pd s interaction. Furthermore, a Pd d_π – π^* interaction can be observed.

Moreover, the XP Pd 3d spectra of Pd/NMC and Pd/CMC were investigated, which help to further understand the metal–support interactions between Pd and the pyridine-like nitrogen species. The deconvoluted Pd 3d spectra are shown in Fig. 12. For Pd/NMC, three different palladium species at 335.2–335.5 eV (Pd1), 336.8 eV (Pd2), and 337.9 eV (Pd3) can be distinguished from the $3d_{5/2}$ portion of the XP Pd 3d spectra. In comparison,

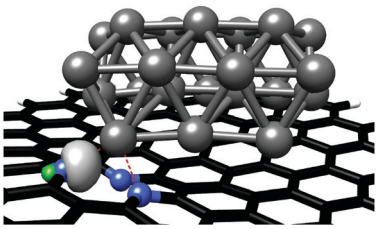


Fig. 11 Visualization of one N lone pair (IBO) in the pyridinic N support 2 system.

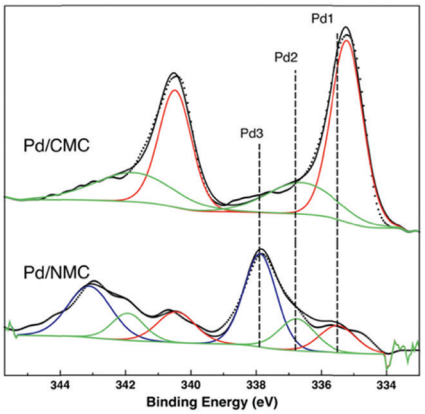


Fig. 12 Pd 3d regions of the deconvoluted XPS results for Pd/CMC and Pd/NMC.

Table 4 Relative abundance (%) of the components in the Pd $3d_{5/2}$ spectra

	Component/binding energy (eV)		
	Pd1	Pd2	Pd3
	335.2	336.8	337.9
Sample	Pd^0	$Pd^{\delta+}$	Pd^{2+}
Pd/NMC	21	25	54
Pd/CMC	68	32	—

only Pd1 and Pd2 are observed for Pd/CMC. The relative abundance of these three species is summarized in Table 4.

The Pd1 peak (335.2 eV) for Pd/CMC is slightly shifted to a higher binding energy with respect to the reported bulk-like metallic palladium (335.0 eV). Thus, it can be assigned to the Pd^0 nanoparticles with varying extents of interaction with the carbon surface. Compared to that of Pd/CMC, the Pd1 peak for Pd/NMC (335.5 eV) is also slightly shifted to a higher binding energy by around 0.3 eV, which can be attributed to more pronounced final-state effects in small Pd NPs (2–5 nm).[37,38] This observation suggests the predominant existence of smaller Pd nanoparticles in Pd/NMC compared with Pd/CMC. According to our previous study, the Pd2 species is suggested to be located on the surface region of Pd nanoparticles/clusters and is electronically modified by oxygen atoms bound to the surface, resulting in a partial positive charge ($Pd^{\delta+}$).[39]

Compared to the $3d_{5/2}$ part of the XP Pd 3d spectra for Pd/CMC, which is dominated by the Pd1 species, a new Pd3 peak at 337.9 eV is predominant for Pd/NMC. A significant electronic modification by the N dopants is presumably responsible for the change of the Pd oxidation state.[40] Based on our DOS calculations, the new peak can be assigned to a divalent Pd center stabilized by the strong interaction with two pyridine-like N atoms: for the Pd_{21}/pyridinic N support 2 model, in which one Pd atom interacts with two pyridinic N atoms, one 3d orbital (delocalized, but with a main contribution of the Pd atom interacting with two pyridinic N atoms) has a binding energy of 262.6 eV. This is noticeably higher than the binding

This journal is © the Owner Societies 2020

Published on 19 August 2020. Downloaded by Ruhr Universitat Bochum on 9/18/2020 10:13:42 AM.

energies of the remaining 3d orbitals and, furthermore, lies in the region of the Pd 3d orbital energy of an isolated Pd^{2+} atom (a DOS energy of around 262.2 eV). Such high binding energies cannot be observed for the Pd_{21}/carbon, Pd_{21}/graphitic N and Pd_{21}/pyrrolic N support systems (compare Fig. S4, ESI†). These results show that pyridinic nitrogen in the support material stabilizes bifunctional palladium nanoparticles containing both Pd^0 and Pd^{2+} centers.

Our results are in agreement with a previous study, in which Pd^{2+} ions coordinated by nitrogen species of the carbon support were reported based on a study of XPS and NEXAFS[35]. Earlier, Stonkus *et al.*[41] confirmed that the deposition of palladium on N-functionalized carbon nanofibers contributes to a change in the redox properties of Pd as compared to that of Pd on N-free carbon nanofibers.

For Pd/NMC, a better fitting of the N 1s spectrum (Fig. 6) was obtained, assuming the presence of one more type of nitrogen species with a binding energy of 398.9 eV (shifted by 0.9 eV). Based on the DOS for the Pd_{21}/pyridinic N support 2 model showing two different binding energies (one for the two interacting N atoms and one for the non-interacting N atom) separated by around 0.7 eV, this new peak could be assigned to the pyridinic nitrogen species interacting with Pd NPs (the N–Pd component).

This is also in agreement with a study by Bulusheva and coworkers,[36] who also detected a new peak in the same region after depositing single Pd atoms on N-functionalized mesoporous carbon materials. Meanwhile, similar changes in the NEXAFS spectra of nitrogen after Pd deposition were observed and the new species could be assigned to the formation of a bond of palladium atoms with pyridinic nitrogen atoms.

Conclusions

With the combined experimental and computational approach, we were able to identify the preferential adsorption sites of Pd nanoparticles on NMC and, furthermore, to provide an in-depth insight into the corresponding metal–support interactions.

Nitrogen is embedded into the carbon structure in four forms: pyridinic, pyrrolic, graphitic and oxidized or NO-like N species. The majority of the N atoms are in the state of pyridinic and pyrrolic groups. In general, N doping increases the adsorption energy of the Pd clusters, which is, in the first place, an effect of the covalent and electrostatic character. For graphitic nitrogen this effect can be explained by stronger covalent Pd–support bonds due to the additional electron and the charge redistribution introduced by the graphitic N atom. Stronger covalent Pd–support bonds can also be observed for pyrrolic nitrogen, which is mainly caused by a charge redistribution.

According to our XPS and DFT results, pyridinic nitrogen atoms are the preferential adsorption sites for Pd nanoparticles on NMC. When a Pd cluster is adsorbed on pyridinic nitrogen, two N atoms interact with one Pd atom *via* an N-LP – Pd d_σ and an N-LP – Pd s as well as a Pd d_π – π^* charge transfer. This interaction results in a change in the Pd oxidation state and leads to a bifunctional palladium nanoparticle containing Pd^0 and Pd^{2+} centers.

In summary nitrogen-doped mesoporous carbon can effectively anchor Pd nanoparticles, especially due to strong interactions with pyridinic nitrogen atoms. These results raise the question of how N doping affects the catalytic hydrogenation reactions on carbon-supported Pd nanoparticles. As the majority of the N atoms are in the state of pyridinic and pyrrolic groups, which are basic, Pd/NMC should provide moderate to strong surface basicity, desired for highly selective and effective hydrogenation reactions. Furthermore, the coexistence of Pd^0 and Pd^{2+} centers is expected to influence the mechanisms of these reactions.

Conflicts of interest

The authors declare no competing financial interest.

Acknowledgements

The authors gratefully acknowledge the financial support by Deutsche Forschungsgemeinschaft within the framework of the Sino-German initiative ''Novel Functional Materials for Sustainable Chemistry'' through grant Ha 2588/9-1, by Deutsche Forschungsgemeinschaft (grant MU 1327/10-1) and by the Max Planck society (Max Planck fellowship).

References

1 K. P. De Jong and J. W. Geus, Carbon Nanofibers: Catalytic Synthesis and Applications, *Catal. Rev.*, 2000, **42**(4), 481–510.
2 C. Li, A. Zhao, W. Xia, C. Liang and M. Muhler, Quantitative Studies on the Oxygen and Nitrogen Functionalization of Carbon Nanotubes Performed in the Gas Phase, *J. Phys. Chem. C*, 2012, **116**(39), 20930–20936.
3 Y. a. Huang, F. Yang, Z. Xu and J. Shen, Nitrogen-containing mesoporous carbons prepared from melamine formaldehyde resins with $CaCl_2$ as a template, *J. Colloid Interface Sci.*, 2011, **363**(1), 193–198.
4 W. Xia, Interactions between metal species and nitrogen-functionalized carbon nanotubes, *Catal. Sci. Technol.*, 2016, **6**(3), 630–644.
5 V. Kratky, M. Kralik, M. Mecarova, M. Stolcova, L. Zalibera and M. Hronec, Effect of catalyst and substituents on the hydrogenation of chloronitrobenzenes, *Appl. Catal., A*, 2002, **235**(1), 225–231.
6 L. Warczinski and C. Hättig, A quantum chemical study of hydrogen adsorption on carbon-supported palladium clusters, *Phys. Chem. Chem. Phys.*, 2019, **21**(38), 21577–21587.
7 Y. a. Huang, S. Hu, S. Zuo, Z. Xu, C. Han and J. Shen, Mesoporous carbon materials prepared from carbohydrates with a metal chloride template, *J. Mater. Chem.*, 2009, **19**(41), 7759–7764.

Published on 19 August 2020. Downloaded by Ruhr Universitat Bochum on 9/18/2020 10:13:42 AM.

8 S. Alijani, S. Capelli, S. Cattaneo, M. Schiavoni, C. Evangelisti, K. M. H. Mohammed, P. P. Wells, F. Tessore and A. Villa, Capping Agent Effect on Pd-Supported Nanoparticles in the Hydrogenation of Furfural, *Catalysts*, 2020, **10**(1), 11.
9 R. Redón, S. K. Rendón-Lara, A. L. Fernández-Osorio and V. Ugalde-Saldívar, Aerobic Synthesis of Palladium Nanoparticles, *Rev. Adv. Mater. Sci.*, 2011, **27**, 31–42.
10 B. Hu, L. Warczinski, Q. Fu, M. Lu, M. Li, C. Hättig, M. Muhler and B. Peng, Selective Hydrogenolysis of 5-Hydroxymethylfurfural to 2,5-Dimethylfuran by Formic Acid over Pd Supported on N-doped Mesoporous Carbon, 2020, under review.
11 J. Tao, J. P. Perdew, V. N. Staroverov and G. E. Scuseria, Climbing the Density Functional Ladder: Nonempirical Meta-Generalized Gradient Approximation Designed for Molecules and Solids, *Phys. Rev. Lett.*, 2003, **91**(14), 146401.
12 F. Weigend and R. Ahlrichs, Balanced basis sets of split valence, triple zeta valence and quadruple zeta valence quality for H to Rn: Design and assessment of accuracy, *Phys. Chem. Chem. Phys.*, 2005, **7**(18), 3297–3305.
13 Turbomole V7.3 2018, a development of University of Karlsruhe and Forschungszentrum Karlsruhe GmbH, 1989–2007, TURBOMOLE GmbH, since 2007, available from http://www.turbomole.com.
14 D. Andrae, U. Häußermann, M. Dolg, H. Stoll and H. Preuß, Energy-adjusted *ab initio* pseudopotentials for the second and third row transition elements, *Theor. Chim. Acta*, 1990, **77**(2), 123–141.
15 M. Sierka, A. Hogekamp and R. Ahlrichs, Fast evaluation of the Coulomb potential for electron densities using multipole accelerated resolution of identity approximation, *J. Chem. Phys.*, 2003, **118**(20), 9136–9148.
16 F. Weigend, Accurate Coulomb-fitting basis sets for H to Rn, *Phys. Chem. Chem. Phys.*, 2006, **8**(9), 1057–1065.
17 S. Grimme, J. Antony, S. Ehrlich and H. Krieg, A consistent and accurate *ab initio* parametrization of density functional dispersion correction (DFT-D) for the 94 elements H-Pu, *J. Chem. Phys.*, 2010, **132**(15), 154104.
18 A. E. Reed, R. B. Weinstock and F. Weinhold, Natural population analysis, *J. Chem. Phys.*, 1985, **83**(2), 735–746.
19 G. Knizia, Intrinsic Atomic Orbitals: An Unbiased Bridge between Quantum Theory and Chemical Concepts, *J. Chem. Theory Comput.*, 2013, **9**(11), 4834–4843.
20 K. A. Peterson, D. Figgen, M. Dolg and H. Stoll, Energy-consistent relativistic pseudopotentials and correlation consistent basis sets for the 4d elements Y–Pd, *J. Chem. Phys.*, 2007, **126**(12), 124101.
21 R. S. Mulliken, Electronic Population Analysis on LCAO–MO Molecular Wave Functions. I, *J. Chem. Phys.*, 1955, **23**(10), 1833–1840.
22 A. Schäfer, C. Huber and R. Ahlrichs, *J. Chem. Phys.*, 1994, **100**, 5829.
23 N. Pueyo Bellafont, F. Illas and P. S. Bagus, Validation of Koopmans' theorem for density functional theory binding energies, *Phys. Chem. Chem. Phys.*, 2015, **17**(6), 4015–4019.
24 P. S. Bagus, Self-Consistent-Field Wave Functions for Hole States of Some Ne-Like and Ar-Like Ions, *Phys. Rev.*, 1965, **139**(3A), A619–A634.
25 J. M. Kahk and J. Lischner, Core electron binding energies of adsorbates on Cu(111) from first-principles calculations, *Phys. Chem. Chem. Phys.*, 2018, **20**(48), 30403–30411.
26 Z. Luo, S. Lim, Z. Tian, J. Shang, L. Lai, B. MacDonald, C. Fu, Z. Shen, T. Yu and J. Lin, Pyridinic N doped graphene: synthesis, electronic structure, and electrocatalytic property, *J. Mater. Chem.*, 2011, **21**(22), 8038–8044.
27 I. Matanovic, K. Artyushkova, M. B. Strand, M. J. Dzara, S. Pylypenko and P. Atanassov, Core Level Shifts of Hydrogenated Pyridinic and Pyrrolic Nitrogen in the Nitrogen-Containing Graphene-Based Electrocatalysts: In-Plane *vs*. Edge Defects, *J. Phys. Chem. C*, 2016, **120**(51), 29225–29232.
28 J. J. Adjizian, P. De Marco, I. Suarez-Martinez, A. A. El Mel, R. Snyders, R. Y. N. Gengler, P. Rudolf, X. Ke, G. Van Tendeloo, C. Bittencourt and C. P. Ewels, Platinum and palladium on carbon nanotubes: Experimental and theoretical studies, *Chem. Phys. Lett.*, 2013, **571**, 44–48.
29 T. Prasomsri, D. Shi and D. E. Resasco, Anchoring Pd nanoclusters onto pristine and functionalized single-wall carbon nanotubes: A combined DFT and experimental study, *Chem. Phys. Lett.*, 2010, **497**(1), 103–107.
30 W. Sun, Z. Liu, C. Jiang, Y. Xue, W. Chu and X. Zhao, Experimental and theoretical investigation on the interaction between palladium nanoparticles and functionalized carbon nanotubes for Heck synthesis, *Catal. Today*, 2013, **212**, 206–214.
31 J. Cai, S. Bennici, J. Shen and A. Auroux, Influence of N addition in mesoporous carbons used as supports of Pt, Pd and Ru for toluene hydrogenation and iron oxide for benzene oxidation, *React. Kinet., Mech. Catal.*, 2015, **115**(1), 263–282.
32 M. Figueras, I. J. Villar-Garcia, F. Viñes, C. Sousa, V. A. de la Peña O'Shea and F. Illas, Correcting Flaws in the Assignment of Nitrogen Chemical Environments in N-Doped Graphene, *J. Phys. Chem. C*, 2019, **123**(17), 11319–11327.
33 E. Raymundo-Piñero, D. Cazorla-Amorós and A. Linares-Solano, The role of different nitrogen functional groups on the removal of SO_2 from flue gases by N-doped activated carbon powders and fibres, *Carbon*, 2003, **41**(10), 1925–1932.
34 J. J. Yeh and I. Lindau, Atomic subshell photoionization cross sections and asymmetry parameters: $1 \leq Z \leq 103$, *At. Data Nucl. Data Tables*, 1985, **32**(1), 1–155.
35 W. B. Schneider, U. Benedikt and A. A. Auer, Interaction of Platinum Nanoparticles with Graphitic Carbon Structures: A Computational Study, *ChemPhysChem*, 2013, **14**(13), 2984–2989.
36 D. A. Bulushev, M. Zacharska, E. V. Shlyakhova, A. L. Chuvilin, Y. Guo, S. Beloshapkin, A. V. Okotrub and L. G. Bulusheva, Single Isolated Pd^{2+} Cations Supported on N-Doped Carbon as Active Sites for Hydrogen Production from Formic Acid Decomposition, *ACS Catal.*, 2016, **6**(2), 681–691.
37 R. Arrigo, M. E. Schuster, Z. Xie, Y. Yi, G. Wowsnick, L. L. Sun, K. E. Hermann, M. Friedrich, P. Kast, M. Hävecker, A. Knop-Gericke and R. Schlögl, Nature of the N–Pd Interaction in Nitrogen-Doped Carbon Nanotube Catalysts, *ACS Catal.*, 2015, **5**(5), 2740–2753.

 This journal is © the Owner Societies 2020

Published on 19 August 2020. Downloaded by Ruhr Universitat Bochum on 9/18/2020 10:13:42 AM.

38 R. Arrigo, M. E. Schuster, S. Abate, S. Wrabetz, K. Amakawa, D. Teschner, M. Freni, G. Centi, S. Perathoner, M. Hävecker and R. Schlögl, Dynamics of Palladium on Nanocarbon in the Direct Synthesis of H_2O_2, *ChemSusChem*, 2014, **7**(1), 179–194.

39 P. Chen, A. Khetan, F. Yang, V. Migunov, P. Weide, S. P. Stürmer, P. Guo, K. Kähler, W. Xia, J. Mayer, H. Pitsch, U. Simon and M. Muhler, Experimental and Theoretical Understanding of Nitrogen-Doping-Induced Strong Metal–Support Interactions in Pd/TiO_2 Catalysts for Nitrobenzene Hydrogenation, *ACS Catal.*, 2017, **7**(2), 1197–1206.

40 J. Graciani, A. Nambu, J. Evans, J. A. Rodriguez and J. F. Sanz, Au ↔ N Synergy and N-Doping of Metal Oxide-Based Photocatalysts, *J. Am. Chem. Soc.*, 2008, **130**(36), 12056–12063.

41 O. A. Stonkus, L. S. Kibis, O. Yu. Podyacheva, E. M. Slavinskaya, V. I. Zaikovskii, A. H. Hassan, S. Hampel, A. Leonhardt, Z. R. Ismagilov, A. S. Noskov and A. I. Boronin, Palladium Nanoparticles Supported on Nitrogen-Doped Carbon Nanofibers: Synthesis, Microstructure, Catalytic Properties, and Self-Sustained Oscillation Phenomena in Carbon Monoxide Oxidation, *ChemCatChem*, 2014, **6**(7), 2115–2128.